Acoustic Metagrating Holograms

Hong-Yu Zou, Yong Ge, Ke-Qi Zhao, Yu-Jing Lu, Qiao-rui Si, Shou-Qi Yuan, Hongsheng Chen, Hong-Xiang Sun, Yihao Yang,* and Baile Zhang**

Dr. H.-Y. Zou, Dr. Y. Ge, Mr. K.-Q. Zhao, Dr. Y.-J. Lu, Dr. Q.-R. Si, Prof. S.-Q. Yuan, Prof. H.-X. Sun

Research Center of Fluid Machinery Engineering and Technology, School of Physics and Electronic Engineering, Jiangsu University, Zhenjiang 212013, China.
E-mail: jsdxshx@ujs.edu.cn (H.-X. S.)

Prof. H.-X. Sun

State Key Laboratory of Acoustics, Institute of Acoustics, Chinese Academy of Sciences, Beijing 100190, China.

Prof. H. S. Chen, Prof. Y. H. Yang

Interdisciplinary Center for Quantum Information, State Key Lab. of Modern Optical Instrumentation, College of Information Science and Electronic Engineering, Zhejiang University, Hangzhou 310027, China.
E-mail: yangyihao@zju.edu.cn (Y. H. Y.)

Prof. H. S. Chen, Prof. Y. H. Yang

ZJU-Hangzhou Global Science and Technology Innovation Center, Key Laboratory of Advanced Micro/Nano Electronic Devices & Smart Systems of Zhejiang, ZJU-UIUC Institute, Zhejiang University, Hangzhou 310027, China.

Prof. B. L. Zhang

Division of Physics and Applied Physics, School of Physical and Mathematical Sciences, Nanyang Technological University, 21 Nanyang Link, Singapore 637371, Singapore.
E-mail: blzhang@ntu.edu.sg (B. L. Z.)

Prof. B. L. Zhang

Centre for Disruptive Photonic Technologies, The Photonics Institute, Nanyang Technological University, 50 Nanyang Avenue,Singapore 639798, Singapore.

Metasurface holograms represent a common category of metasurface devices that utilize in-plane phase gradients to shape wavefronts, forming holographic images through the application of the generalized Snell's law (GSL). While conventional metasurfaces focus solely on phase gradients, metagratings, which incorporate higher-order wave diffraction, further expand the GSL's generality. Recent advances in certain acoustic metagratings have demonstrated an updated GSL extension capable of reversing anomalous transmission and reflection, whose reversal is characterized by the parity of the number of wave propagation trips through the metagrating. However, the current extension of GSL has remained limited to one-dimensional metagratings, unable to access two-dimensional (2D) holographic images in three-dimensional (3D) spaces. Here, we investigate the GSL extension to 2D metagratings for manipulating waves within 3D spaces. Through our analysis, we experimentally demonstrate a series of acoustic metagrating holograms. These holographic images exhibit the unique ability to switch between transmission and reflection types independently. Our study introduces an additional dimension to modern holography design and metasurface wavefront manipulation.

Over the past decades, the generalized Snell's law (GSL)[1] has attacted significant attention within the realms of both physics and engineering, and paved the way for complex wavefront manipulation in photonics,[2-9] mechanics,[10-17] and acoustics.[18-26] In acoustics, the combination of the GSL and metasurfaces, a type of artificial phased structures of ultrathin thicknesses, has been demonstrated substantial potential in a variety of application scenarios, one of which is metasurface holograms. Based on the GSL, holographic metasurfaces can store the phase profile of the desired wavefront. With the excitation of incident wave, the wavefront can be reconstructed to form the designed holographic image.[27-31] Generally, in the manipulation of acoustic wavefront based on the GSL, when the incident angle approaches a critical angle, the output energy will become evanescent.[1] However, under certain special conditions, sound refraction/reflection can be still observed, even when the incident angle surpasses the critical range.[32] Such a phenomenon cannot be captured by the theoretical framework of the GSL, which manifests a fundamental limitation of the GSL.

Recently, another class of artificial planar structures, called metagratings, have been proposed and demonstrated.[33-37] The metagrating structures can effectively manipulate sound energy in a single direction, and simultaneously suppress output waves of undesired diffraction orders, resulting in high-performance sound refraction or reflection devices.[32] Subsequently, by periodically arranging supercells, gradient-phase acoustic metagratings (AMs) have been designed and experimentally studied,[38-42] in which anomalous sound refraction or reflection can be observed under a full-angle incidence owing to the synergy effect between sound diffraction and phase modulation.[43] To theoretically explain this phenomenon, an additional term of sound diffraction has been added in the GSL,[32] effectively overcoming the fundamental limitation of critical incident angles for the GSL. Additionally, following the GSL extension, final states of sound refraction or reflection caused by the gradient-phase AMs can also be predicted by the parity of the number of round trips for wave propagation in each phased unit cell.[44-46] Practically, to design different types of acoustic functional devices, it generally requires the realization of AMs with aperiodic phase profiles, which have also been discussed in the context of the GSL extension.[47,48] However, the studies on the GSL extension have been predominantly focused on sound manipulation with one-dimensional periodic or aperiodic AMs in two-dimensional (2D) space, which poses challenges for applications in multifunctional sound devices with practical use in three-dimensional (3D) space, such as acoustic holography.

In this work, we theoretically extend the GSL to 3D space, and experimentally design multiple 2D dual-layer aperiodic AMs. The proposed aperiodic AMs can be used to achieve sound refraction or reflection in 3D space, which can be well predicted by the GSL extension, and effectively overcomes the limitation of critical ranges in the GSL. Moreover, the designed 2D dual-layer aperiodic AMs can also enable the reversal of transmitted and reflected complex wavefront modulation. As a proof of concept, we design a series of 2D dual-layer aperiodic AMs. By sticking and separating the AMs, we experimentally observe the conversion between sound abnormal refraction and reflected holographic images, as well as that between transmitted and reflected holographic images of various letters. The measured results agree well with the theoretical and simulated counterparts, which provide the feasibility of designing advanced 3D acoustic devices with practical applications.

As schematically illustrated in **Figure 1**a, we design a type of 2D dual-layer aperiodic AMs. When a cylindrical acoustic wave impinges on the stuck 2D dual-layer aperiodic AMs, the sound energy can transmit through both AMs, and form a transmitted holographic image of the letter "U". However, by separating the dual-layer AMs (shown in Figure 1b), the sound energy is unable to penetrate the structure, and is reflected as the image of the letter "S". Thus, by simply sticking and separating the dual-layer AMs, one can achieve the reversal of the transmitted and reflected acoustic holography. Here, it is worth noting that the metasurface structures can only realize a single function of transmitted or reflected hologram based on the GSL. Thus, such a phenomenon cannot be obtained by using the acoustic metasurfaces based on the GSL.

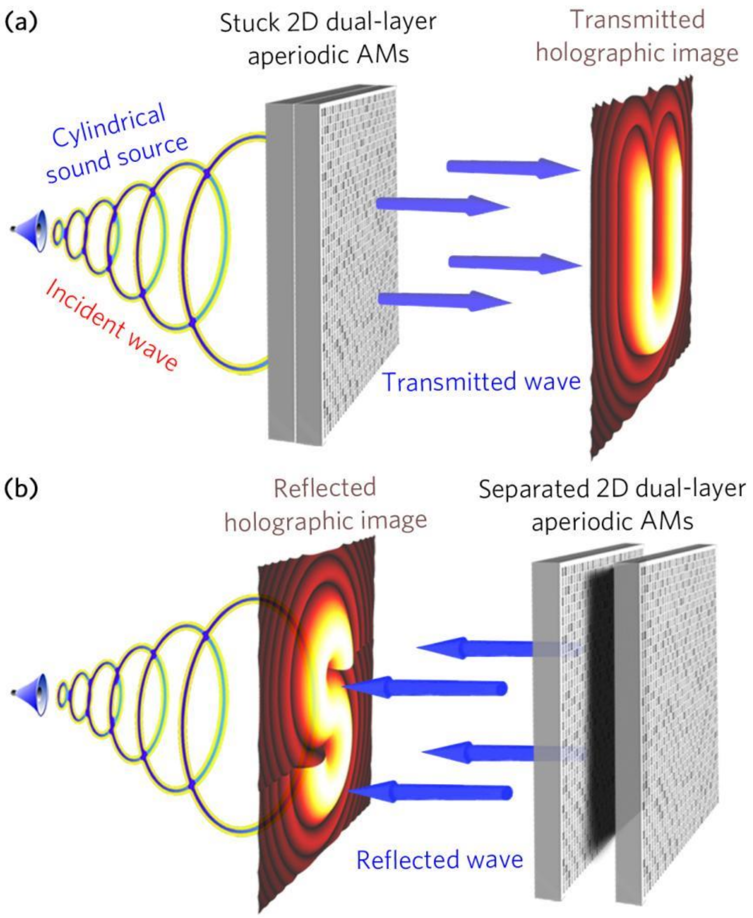

Figure 1. Schematic of the reversal of a) transmitted and b) reflected acoustic holography by sticking and separating dual-layer aperiodic AMs. The blue arrows represent the directions of the transmitted/reflected waves.

As shown in **Figure 2**, to realize it, we start with the design of a single 2D aperiodic AM composed of phased unit cells with a size of $l_x \times l_y \times l_z$ (Figure 2a). The phase profile of the aperiodic AM is $\varphi(x, y)$ (the upper inset of Figure 2b), thus the phase gradients in the x and y directions can be expressed as

$$\begin{cases} \dfrac{\partial\varphi}{\partial x} = \dfrac{1}{l_x}\left[\varphi(x+l_x, y) - \varphi(x, y)\right] \\ \dfrac{\partial\varphi}{\partial y} = \dfrac{1}{l_y}\left[\varphi(x, y+l_y) - \varphi(x, y)\right] \end{cases}, \tag{1}$$

Assuming that an incident acoustic wave with the wave vectors of k_x^{i} and k_y^{i} impinges on the aperiodic AM, and the transmitted wave with the wave vectors of k_x^{t} and k_y^{t} can be predicted based on the GSL,[49] which can be written as

$$\begin{cases} k_x^{\mathrm{t}} - k_x^{\mathrm{i}} = \dfrac{\partial \varphi}{\partial x} \\ k_y^{\mathrm{t}} - k_y^{\mathrm{i}} = \dfrac{\partial \varphi}{\partial y} \end{cases}, \tag{2}$$

Based on Equation (2), we can obtain that the sound transmission only exists when the incident wave vector k_x^{i} and k_y^{i} are in the critical range $\left(k_x^{\mathrm{i}} + \dfrac{\partial \varphi}{\partial x}\right)^2 + \left(k_y^{\mathrm{i}} + \dfrac{\partial \varphi}{\partial y}\right)^2 \leq k_0^2$ (k_0 is the airborne wave number); otherwise, the transmitted wave vector in the *z* direction becomes imaginary, indicating that the sound energy is evanescent.[1] In this case, the evanescent sound energy propagates back and forth inside each unit cell until the *n*-times round trip of sound propagation satisfies the m_x-order and m_y-order diffractions in the *x* and *y* directions,[44] resulting in sound transmission or reflection (the bottom inset of Figure 2a). Thus, the phase differences between the neighbouring unit cells in the *x* and *y* directions must be equal to $2\pi m_x$ and $2\pi m_y$ based on the diffraction law (the bottom inset of Figure 2b), which can be expressed as

$$\begin{cases} k_0\left(d_x^{\mathrm{i}} - d_x^{\mathrm{t}}\right) + n\left[\varphi(x + l_x, y) - \varphi(x, y)\right] = 2\pi m_x \\ k_0\left(d_y^{\mathrm{i}} - d_y^{\mathrm{t}}\right) + n\left[\varphi(x, y + l_y) - \varphi(x, y)\right] = 2\pi m_y \end{cases}, \tag{3}$$

where d_x^{i}, d_y^{i}, d_x^{t} and d_y^{t} represent the differences of propagation distances between the incident and transmitted waves in the *x* and *y* directions. The relationships between $\theta_{\mathrm{i(t)}}$, $\beta_{\mathrm{i(t)}}$, $d_x^{\mathrm{i(t)}}$ and $d_y^{\mathrm{i(t)}}$ are

$$\begin{cases} d_x^{\mathrm{i(t)}} = l_x \sin\theta_{\mathrm{i(t)}} \cos\beta_{\mathrm{i(t)}} \\ d_y^{\mathrm{i(t)}} = l_y \sin\theta_{\mathrm{i(t)}} \sin\beta_{\mathrm{i(t)}} \end{cases}, \tag{4}$$

where $\theta_{\mathrm{i(t)}}$ represents the incident (transmitted) polar angle measured from the +*z* direction ($0 \leq \theta_{\mathrm{i(t)}} \leq \pi/2$), and $\beta_{\mathrm{i(t)}}$ is the corresponding azimuth angle measured from the +*x* direction in the *x*-*y* plane ($-\pi \leq \beta_{\mathrm{i(t)}} \leq \pi$). Here, we can get $k_x^{\mathrm{i(t)}} = k_0 \sin\theta_{\mathrm{i(t)}} \cos\beta_{\mathrm{i(t)}}$ and $k_y^{\mathrm{i(t)}} = k_0 \sin\theta_{\mathrm{i(t)}} \sin\beta_{\mathrm{i(t)}}$. Thus, Equation (4) can be rewritten as

$$\begin{cases} k_0 d_x^{\mathrm{i(t)}} = k_x^{\mathrm{i(t)}} l_x \\ k_0 d_y^{\mathrm{i(t)}} = k_y^{\mathrm{i(t)}} l_y \end{cases}. \tag{5}$$

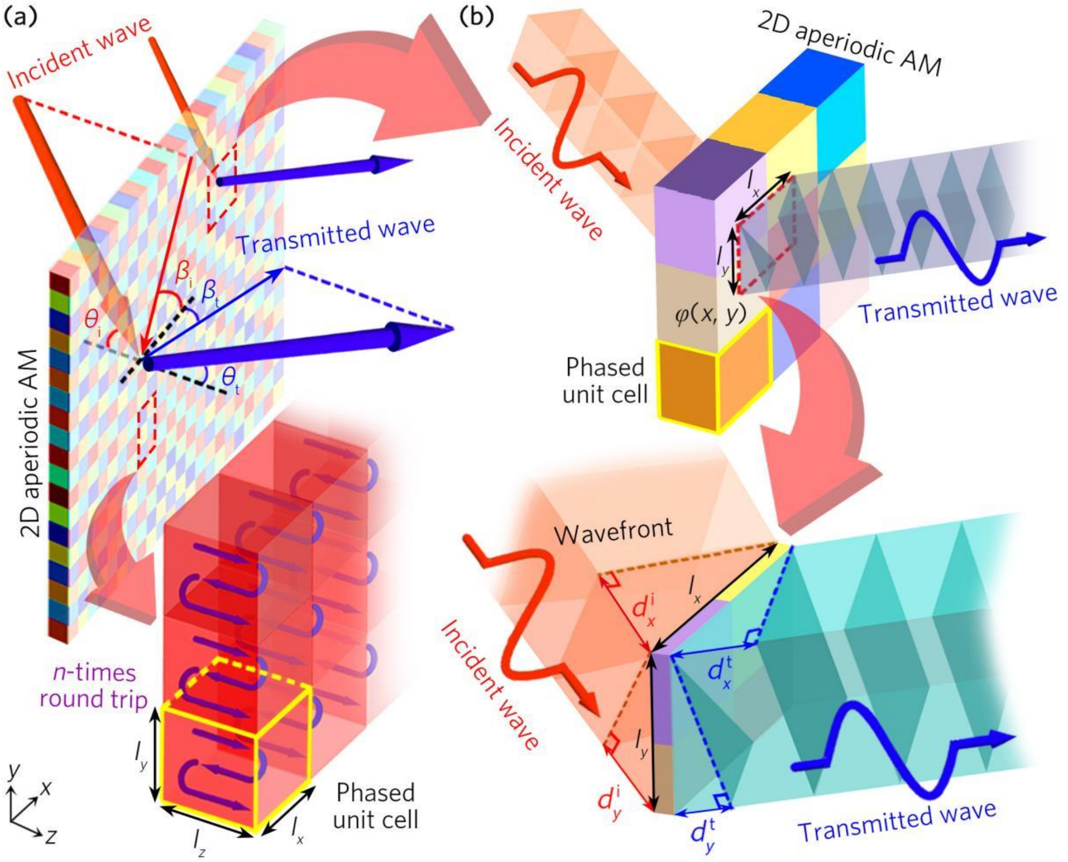

Figure 2. a) Schematic of a 2D aperiodic AM composed of phased unit cells. The bottom inset depicts n-times round trip of sound propagation inside each unit cell. b) Schematic of the deduction of the GSL extension in 3D space for the 2D aperiodic AMs.

To provide an insight into the influence of n on sound propagation, we here take 2D periodic AMs with the constant phase gradients $\frac{\partial \varphi}{\partial x} = \xi_x$ and $\frac{\partial \varphi}{\partial y} = \xi_y$ as an example, and theoretically derive the relationship between the parity of n and transmittance/reflectance based on the effective medium theory (see the Supporting Information). We can see that, when n is odd/even, the sound transmission/reflection can be achieved by the AM. Thus, the final state of sound transmission and reflection in 3D space is determined by the parity of n, which is markedly different from that of the acoustic metasurfaces. Such a characteristic is also equally applicable to the 2D aperiodic AMs. Therefore, by substituting Equations (1) and (5) into Equation (3), the

GSL extension for the sound transmission and reflection caused by the 2D aperiodic AMs can be expressed as

$$\begin{cases} k_x^{\mathrm{t}} - k_x^{\mathrm{i}} = n\dfrac{\partial\varphi}{\partial x} - 2\pi\dfrac{m_x}{l_x} \\ k_y^{\mathrm{t}} - k_y^{\mathrm{i}} = n\dfrac{\partial\varphi}{\partial y} - 2\pi\dfrac{m_y}{l_y} \end{cases} (n \text{ is odd}), \tag{6}$$

$$\begin{cases} k_x^{\mathrm{r}} - k_x^{\mathrm{i}} = n\dfrac{\partial\varphi}{\partial x} - 2\pi\dfrac{m_x}{l_x} \\ k_y^{\mathrm{r}} - k_y^{\mathrm{i}} = n\dfrac{\partial\varphi}{\partial y} - 2\pi\dfrac{m_y}{l_y} \end{cases} (n \text{ is even}), \tag{7}$$

where k_x^{r} and k_y^{r} are the reflected wave vectors in the x and y directions, respectively. By introducing the reflected polar angle θ_{r} (measured from the $-z$ direction, $0\leq\theta_{\mathrm{r}}\leq\pi/2$) and the reflected azimuth angle β_{r} (measured from the $+x$ direction in the x-y plane, $-\pi\leq\beta_{\mathrm{r}}\leq\pi$), k_x^{r} and k_y^{r} can be rewritten as $k_x^{\mathrm{r}} = k_0 \sin\theta_{\mathrm{r}} \cos\beta_{\mathrm{r}}$ and $k_y^{\mathrm{r}} = k_0 \sin\theta_{\mathrm{r}} \sin\beta_{\mathrm{r}}$, respectively. Additionally, based on the principle of the minimum propagation path, the parameter n is selected as the minimum value in all solutions which satisfy the condition

$$\left(k_x^{\mathrm{i}} + n\frac{\partial\varphi}{\partial x} - 2\pi\frac{m_x}{l_x}\right)^2 + \left(k_y^{\mathrm{i}} + n\frac{\partial\varphi}{\partial y} - 2\pi\frac{m_y}{l_y}\right)^2 \leq k_0^2, \tag{8}$$

and so do the parameters $|m_x|$ and $|m_y|$ based on the classical diffraction theory. Here, as shown in Equations (6) and (7), by selecting $m_x=m_y=0$ and $n=1$, the GSL extension can be converted into the GSL.

In term of application, based on Equations (6) and (7), we inversely calculate the phase profile of the 2D aperiodic AM

$$\varphi(x,y) = \frac{1}{n}\left[\varphi^{\mathrm{t(r)}}(x,y) - \varphi^{\mathrm{i}}(x,y) + 2\pi\left(m_x\frac{x}{l_x} + m_y\frac{y}{l_y}\right)\right], \tag{9}$$

where $\varphi^{\mathrm{i(t,r)}}(x,y) = \int k_x^{\mathrm{i(t,r)}}(x,y)\mathrm{d}x + k_y^{\mathrm{i(t,r)}}(x,y)\mathrm{d}y$ is defined as the phase profile of the incident (transmitted/reflected) wave. By selecting the appropriate values of (n, m_x, m_y), and design the desired $\varphi^{\mathrm{i}}(x,y)$ and $\varphi^{\mathrm{t(r)}}(x,y)$ in Equations (9), we can theoretically obtain the phase profile of the 2D aperiodic AM, and thus realizing arbitrary sound transmission, reflection and complex sound modulation in 3D space, such as the reversal of the transmitted and reflected acoustic holography in Figure 1.

To realize the 2D dual-layer aperiodic AMs, we here propose a type of phased unit cell composed of 8 Helmholtz resonators (**Figure 3**a). The structure parameters of the unit cell are selected as $l_x=l_y=d=\lambda_0/3$, $d_1=\lambda_0/60$, $d_2=\lambda_0/30$, and $h=2\lambda_0/3$. The parameters w_1 and w_2 are tunable, which is used to control the phase delay of sound. Here, the central frequency is selected as $f_0=5716$ Hz, corresponding to sound wavelength $\lambda_0=6$ cm in air. Throughout this work, we utilize the module of Pressure Acoustics in the COMSOL Multiphysics software to simulate the propagation of sound. The unit cell is made of epoxy resin, which satisfies the condition of sound-hard boundary in the numerical model. The density and sound velocity of air are selected as $\rho_0=1.21$ kg/m^3 and $c_0=343$ m/s, respectively. Figures 3(b) and 3(c) show the phase delays and transmittances caused by the phased unit cells with different values of w_1 and w_2, respectively. We can see that the phase delay can cover a whole 2π range in the ranges of 0.5 cm $\leq w_1 \leq$ 1.5 cm and 0 $\leq w_2 \leq$ 0.6 cm. Compared with the performance of phased unit cells with 4 Helmholtz resonators, the range of the parameters (w_1, w_2) with high transmittances are much wider for those with 8 Helmholtz resonators (see the Supporting Information). Thus we select the phased unit cells with 8 Helmholtz resonators to design AMs in this work. Here, we select 20 phased unit cells, in which the phase delays are distributed from 0 to 2π with an equal step of π/10, and the transmittances are larger than 0.75 (shown in Figure 3d). The corresponding values of phase delays and transmittances, and excited pressure distributions caused by the 20 unit cells are presented in the Supporting Information.

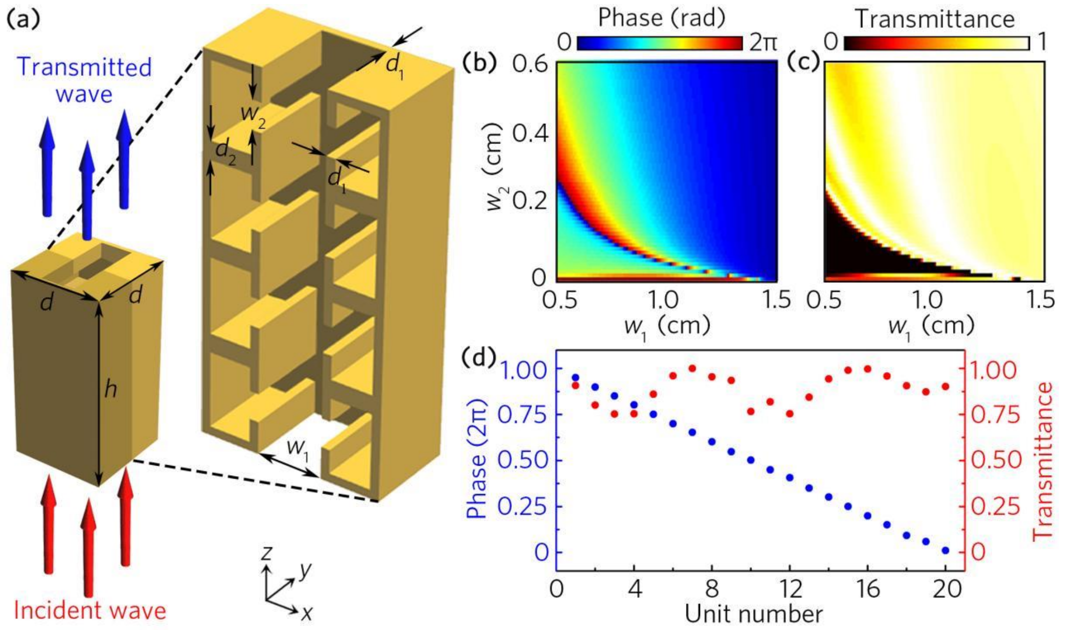

Figure 3. a) 3D view of a phased unit cell. b) Phase delays and c) transmittances caused by the phased unit cells with different values of w_1 and w_2. d) Phase delays and transmittances of 20 selected phased unit cells.

To verify the feasibility of the GSL extension, we design two types of 2D aperiodic AMs with constant phase gradients $\left(\xi_x,\xi_y\right)=\left(\frac{3\sqrt{2}}{5}k_0,\frac{6\sqrt{6}}{7}k_0\right)$ and $\left(\frac{5\sqrt{5}}{8}k_0,\frac{5\sqrt{5}}{7}k_0\right)$. The incident wave vectors are selected as $k_x^{\mathrm{i}}=k_y^{\mathrm{i}}=0$, which are beyond the critical range of GSL. However, the simulated results show that sound abnormal refraction and reflection can be still obtained by AMS1 and AMS2, which match well with the theoretical predictions based on the GSL extension. (see the Supporting Information)

Furthermore, based on the proposed GSL extension, we can achieve the conversion between transmitted and reflected complex wavefront modulation in 3D space by using 2D aperiodic dual-layer AMs. To demonstrate it, we design a type of 2D aperiodic dual-layer AMs (denoted as "AM1" and "AM2"), and realize the reversal of the abnormal refraction and the reflected holographic image of curve as an example. As schematically depicted in **Figure 4**a,b, a cylindrical sound source is positioned at the bottom of the stuck structure of AM1 and AM2 (denoted as "AM1+AM2"), with the distance of l=30cm, and the abnormal refraction with (θ_t, β_t)=(45°, -135°) can be obtained. However, by separating AM1 and AM2, the reflected holographic image of a curve defined by $(x-x_0)^2+(y-y_0)^2=R^2$ is achieved. The center coordinate and radius of the curve are (x_0, y_0)=(25 cm, -25 cm) and R=40 cm, respectively. The distance between the holographic image and AM1 is e=15 cm, and that between AM1 and AM2 is l_1=8 cm.

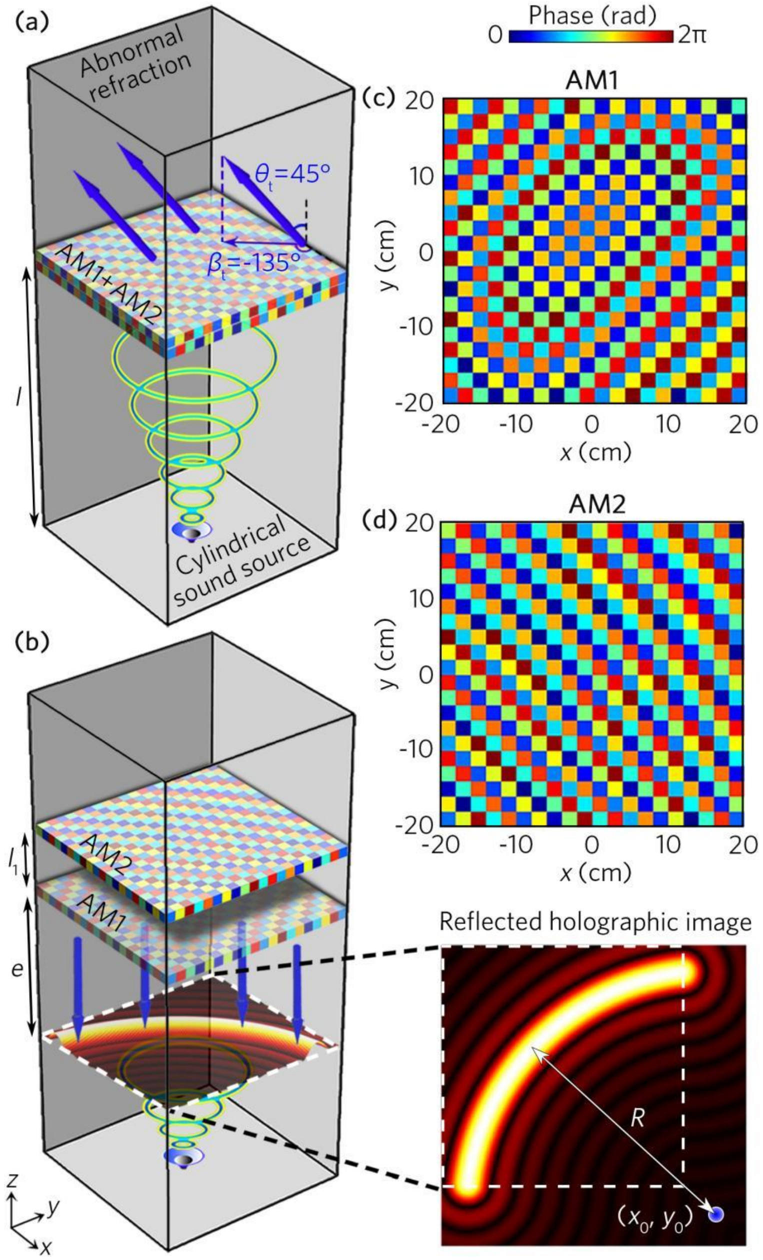

Figure 4. Schematic of the reversal of a) abnormal refraction and b) reflected holographic image of a curve by sticking and separating AM1 and AM2. The incident cylindrical wave is placed at the bottom of AM1. The inset in the lower right corner is the holographic image of a curve. Theoretically calculated phase profiles of c) AM1 and d) AM2.

Here, it is worth noting that the high-order diffractions and multiple times round trip of sound propagation in the unit cell have a certain impact on the performance of wave modulation. We thus select the values of (n, m_x, m_y)=(1, 0, 0) and (2, 1, 1) for the stuck structure of AM1 and AM2 and the separated ones, respectively. Here, the incident angles of the cylindrical wave for (1, 0, 0) are in the critical range of the GSL [Equation (2)]. However, those for (2, 1, 1) are out of range of the critical range, and the corresponding sound modulation can be predicted based on the GSL extension [Equation (7)]. Therefore, based on Equation (9), the phase profiles of the single AM1 and the stuck structures of AM1 and AM2 can be expressed as

$$\varphi_{\mathrm{AM1}}(x,y)=\frac{1}{2}\left[\varphi_2^{\mathrm{r}}(x,y)-\varphi^{\mathrm{i}}(x,y)+3k_0(x+y)\right], \tag{10}$$

$$\varphi_{\mathrm{AM1}}(x,y)+\varphi_{\mathrm{AM2}}(x,y)=\varphi_1^{\mathrm{t}}(x,y)-\varphi^{\mathrm{i}}(x,y). \tag{11}$$

By subtracting Equations (10) and (11), we obtain

$$\varphi_{\mathrm{AM2}}(x,y)=\varphi_1^{\mathrm{t}}(x,y)-\frac{1}{2}\left[\varphi^{\mathrm{i}}(x,y)+\varphi_2^{\mathrm{r}}(x,y)+3k_0(x+y)\right], \tag{12}$$

where the phase profiles of the incident cylindrical wave, the abnormal refraction and the reflected holographic image of the curve are $\varphi^{\mathrm{i}}(x,y)=k_0\sqrt{x^2+y^2+l^2}$, $\varphi_1^{\mathrm{t}}(x,y)=k_0\sin\theta_{\mathrm{t}}(x\cos\beta_{\mathrm{t}}+y\sin\beta_{\mathrm{t}})$, and $\varphi_2^{\mathrm{r}}(x,y)=-k_0\sqrt{\left[\sqrt{(x-x_0)^2+(y-y_0)^2}-R\right]^2+e^2}$, respectively. The corresponding phase profiles are presented in the Supporting Information. Here, to explain the origin of φ_2^{r} and extend it to the holographic image of arbitrary curves, we also provide the detailed derivation in the Supporting Information. Based on Equations (10) and (12), we plot the phase profiles of AM1 and AM2, which are shown in Figure 4c,d, respectively. In addition, the selected values (n, m_x, m_y)=(2, 1, 1) are based on the principle of the minimum propagation path and the classical diffraction theory, which is presented in the Supporting Information.

Figure 5a,b shows the simulated 3D total pressure and intensity distributions, respectively. To demonstrate the theoretical design, we measure and simulate the total pressure distributions on the planes I and II, and the reflected intensity distributions on the planes III and IV, which are presented in the right insets in Figure 5a,b, respectively. We observe that, when AM1 and AM2 are stuck, the incident wave can pass through the structure, and refract as a plane wave with (θ_t, β_t)=(45°, -135°) (blue arrow). Furthermore, we simulate its corresponding far-field intensity distribution (see the Supporting Information). One can see that there exists only a single refracted beam with (θ_t, β_t)=(45°, -135°), indicating that the designed AMs can realize wavefront modulation with high efficiency. On the other hand, it is worth noting that, by separating AM1 and AM2, the modulated waves should be evanescent based on the GSL. However, the sound wave cannot actually transmit AM1. The reflected sound energy is formed as the image of a curve, and is relatively weak in other positions. The measured sound distributions agree well with the simulated results and theoretical designs based on the GSL extension, indicating the feasibility of the reversal of the abnormal refraction and the reflected holographic image based on the dual-layer aperiodic AMs.

Moreover, to exhibit the influence of high values of (n, m_x, m_y) on the performance of wave modulation, we select (n, m_x, m_y)=(3, 1, 1) and (4, 2, 3) for the stuck AM and the separated ones, respectively, and simulate the similar effects as Figure 5. The simulated results present that the transmitted sound energy is slightly weaker and the quality of the reflected holographic image is slightly poorer than those in Figure 5, which are presented in the Supporting Information. Here, we also simulate the intensity distributions on the plane IV for different values of l_1, in which the parameter l_1 has negligible influence on the quality of the reflected holographic image generated by AM1 (see the Supporting Information).

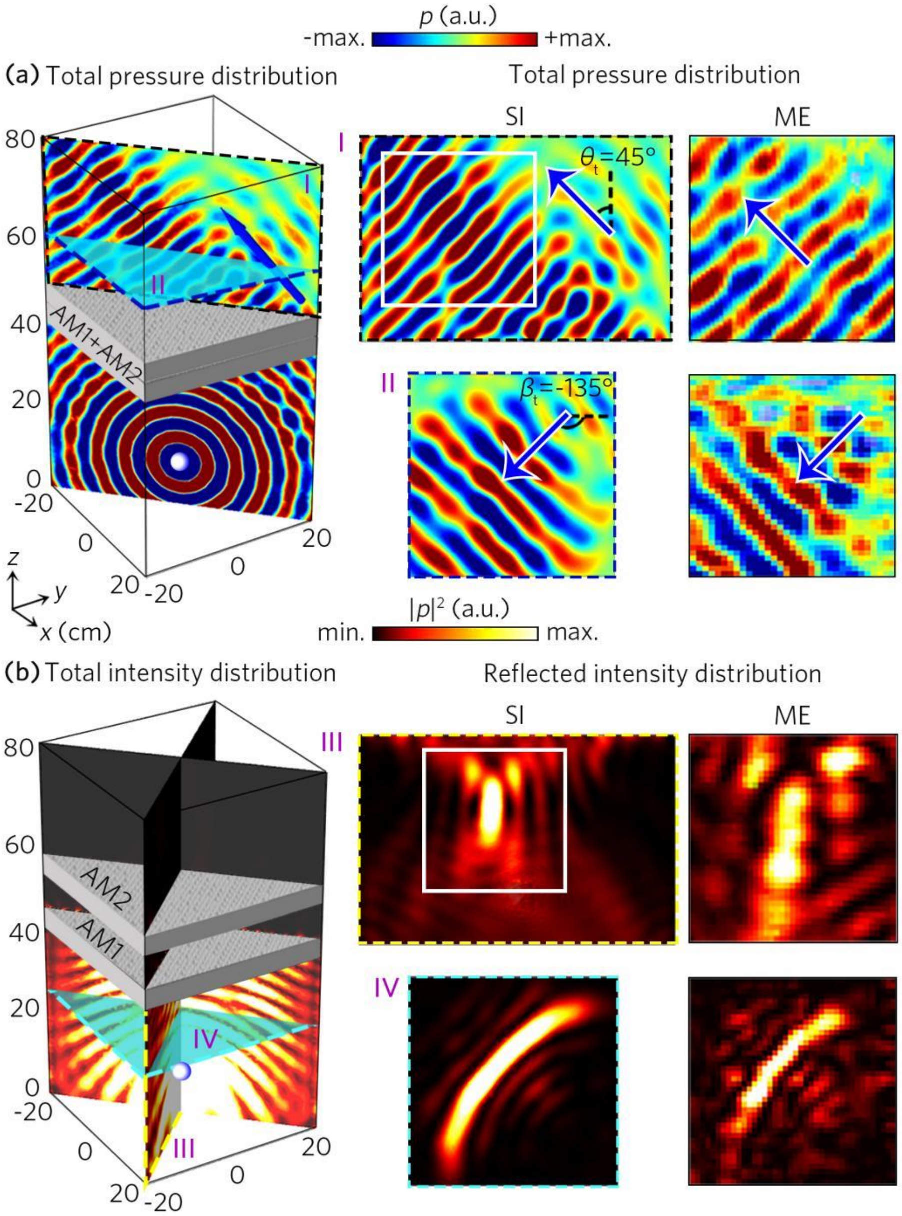

Figure 5. The acoustic a) pressure and b) intensity distributions in 3D space caused by sticking and separating AM1 and AM2. The left panels are simulations in the entire space. The right panels show the corresponding simulated (SI) and measured (ME) results in selected planes: planes I and II in (a) for the pressure distributions, and planes III and IV in (b) for the intensity distributions.

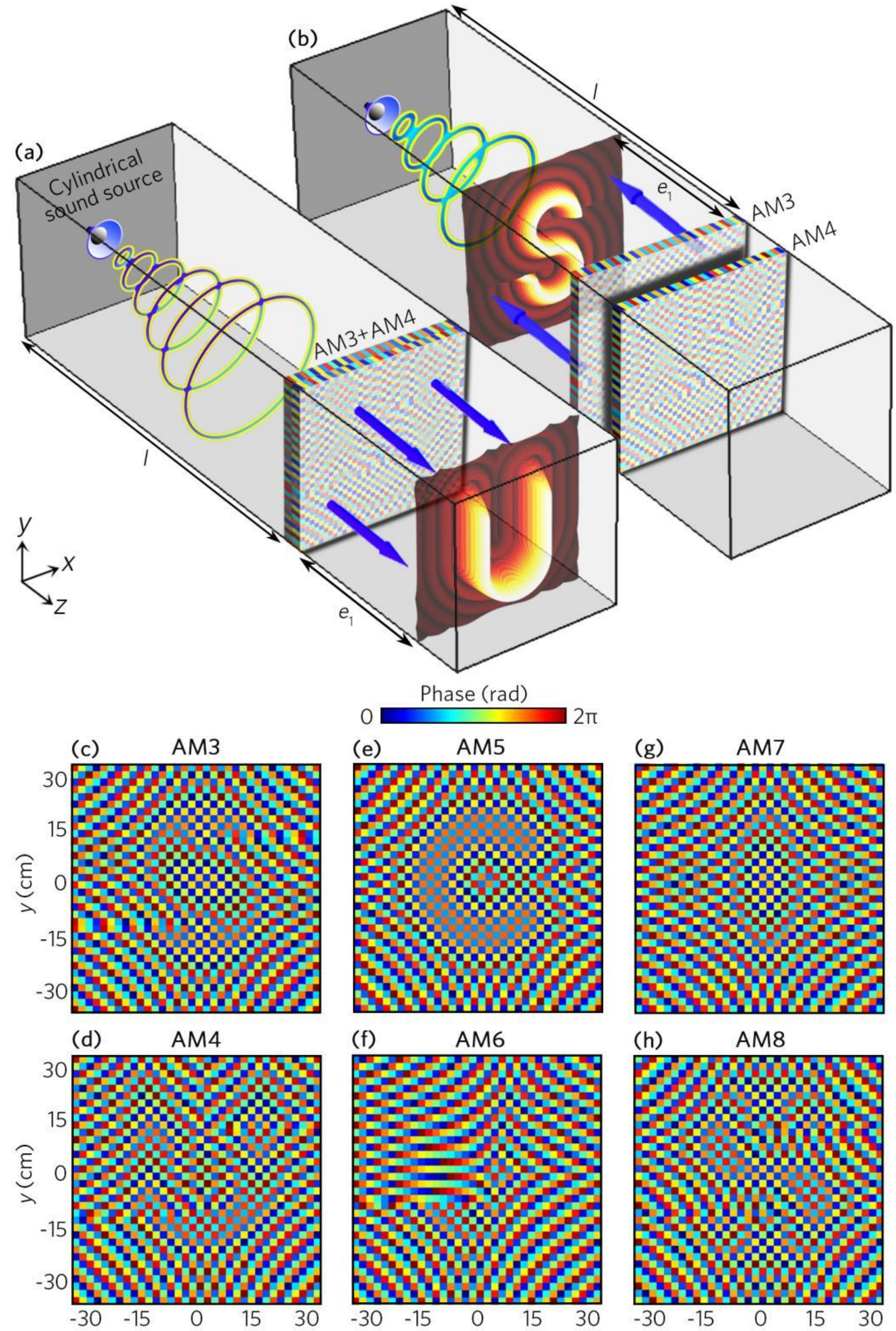

Figure 6. Schematic of the reversal of a) the transmitted holographic image of the letter "U" and b) the reflected holographic image of the letter "S" by sticking and separating the structures of AM3 and AM4. Theoretically calculated phase profiles of c) AM3, d) AM4, e) AM5, f) AM6, g) AM7 and h) AM8.

In addition to the aforementioned results, the proposed 2D dual-layer aperiodic AMs can be used to realize the switch between more complex transmitted and reflected wavefront modulation in 3D space based on the GSL extension. To demonstrate it, we design another 3 types of 2D dual-layer aperiodic AMs, denoted as "AM3" and "AM4", "AM5" and "AM6", "AM7" and "AM8", and experimentally realize the reversal of transmitted holographic images of letters "U", "J", and "S", and reflected images of letters "S", "C", and "I" by separating and sticking AMs. As schematically shown in **Figure 6**a,b, the distance between the cylindrical source and AM is still selected as l=30 cm, and that between the holographic plane and its adjacent AM is e_1=10 cm. Similarly, based on Equation (9), by selecting (n, m_x, m_y)=(2, 1, 1) for reflected holographic images and (n, m_x, m_y)=(1, 0, 0) for transmitted ones, we can theoretically obtain the phase profiles of single AM3, AM5 and AM7, and the stuck structures of AM3 and AM4, AM5 and AM6, and AM7 and AM8, which can be expressed as

$$\varphi_{\mathrm{AM3,5,7}}(x,y)=\frac{1}{2}\left[\varphi^{\mathrm{r}}_{\mathrm{S,C,I}}(x,y)-\varphi^{\mathrm{i}}(x,y)+3k_0(x+y)\right], \tag{13}$$

$$\varphi_{\mathrm{AM4,6,8}}(x,y)=\varphi^{\mathrm{t}}_{\mathrm{U,J,S}}(x,y)-\frac{1}{2}\left[\varphi^{\mathrm{r}}_{\mathrm{S,C,I}}(x,y)+\varphi^{\mathrm{i}}(x,y)+3k_0(x+y)\right], \tag{14}$$

where $\varphi^{\mathrm{t}}_{\mathrm{U}}$, $\varphi^{\mathrm{t}}_{\mathrm{J}}$, $\varphi^{\mathrm{t(r)}}_{\mathrm{S}}$, $\varphi^{\mathrm{r}}_{\mathrm{C}}$ and $\varphi^{\mathrm{r}}_{\mathrm{I}}$ are the phase profiles of the transmitted/reflected holographic images for the letters "U", "J", "S", "C" and "I", whose derivations are similar to that of φ^{r}_{2}. The corresponding phase profiles are shown in the Supporting Information. Based on Equations (13) and (14), we theoretically calculate the phase profiles of AM3-AM8, which are presented in Figure 6c-h, respectively.

Next, we simulate 3D total intensity distributions by sticking and separating AM3 and AM4, AM5 and AM6, AM7 and AM8. The results indicate that the designed AMs have an ability to realize the switch between sound transmission and reflection (see the Supporting Information). To exhibit the performance of acoustic holograms, we further simulate and measure the transmitted total intensity distributions on the holographic planes for the stucked AMs, and reflected ones for the separated AMs, which are shown in **Figure 7**a,b, respectively. We can observe that, when the designed AMs are stuck (denoted as "AM3+AM4", "AM5+AM6" and "AM7+AM8"), the sound energy can pass through AMs, and form the transmitted acoustic holographic images of the letters "U", "J", and "S" (Figure 7a). Additionally, for the separated AMs, most energy is reflected by a single AM3, AM5 and AM7 separately, and thus the transmitted holographic images are converted into the reflected images of the letters "S", "C", and

"I" (Figure 7b). The corresponding measured intensity distributions are presented in the bottom insets of Figure 7a,b, which match well with the simulated ones, showing the feasibility of the conversion between transmitted and reflected acoustic holography by using the dual-layer aperiodic AMs. Here, to quantify the quality of acoustic holograms, we introduce a peak signal-to-noise ratio (PSNR). As examples, we calculate PSNR of the simulated and measured transmitted and reflected holographic images of the letters "U" and "S" at 5716 Hz. The values of PSNR for the holographic images "U" and "S" can reach about 22.89 dB and 25.86 dB in the simulation, and 16.96 dB and 16.33 dB in the measurment, respectively. The simulated values of PSNR are slightly larger than that of a transmitted hologram generated by an acoustic metasurface,[31] indicating a high quality of our acoustic holograms (see the Supporting Information).

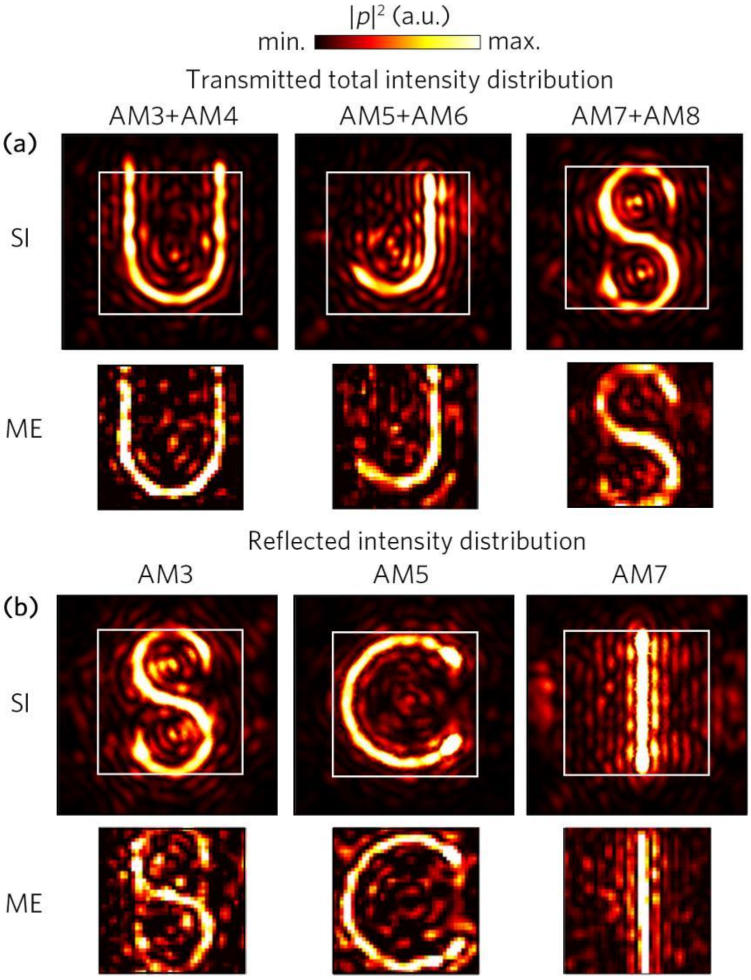

Figure 7. Measured and simulated 2D a) transmitted total intensity distributions of holographic images of the letters "U", "J" and "S", and b) reflected ones of the letters "S", "C" and "I" on the corresponding holographic planes for the stuck and separated AM3 and AM4, AM5 and AM6, AM7 and AM8.

Finally, to quantify the working bandwidth of acoustic holography, we further measure and simulate the total and reflected intensity distributions on the holographic planes at 5466, 5616 and 5766 Hz, which are shown in **Figure 8**a-c, respectively. We can observe that the conversions between the transmitted holographic images of letters “U”, “J” and “S” and the reflected images of letters “S”, “C” and “I” still exist obviously at the 3 frequencies.

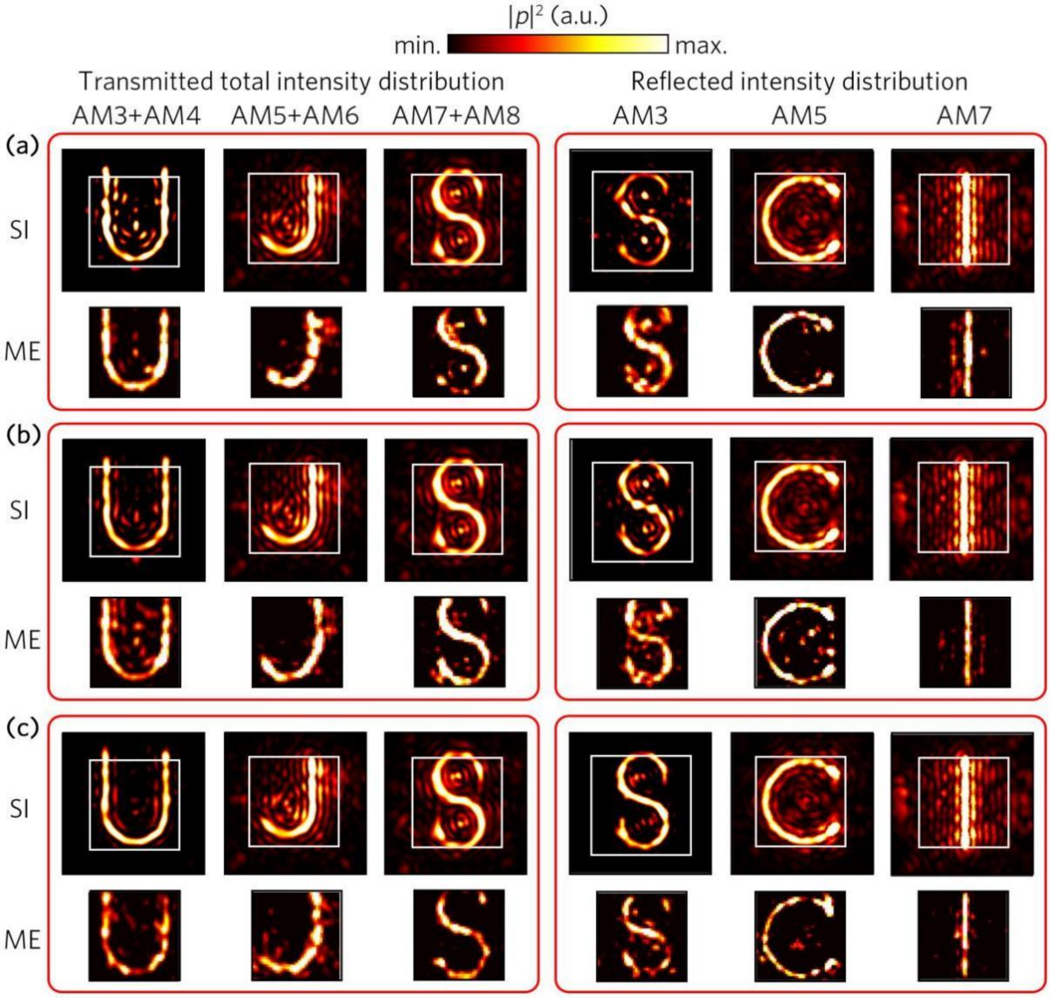

Figure 8. Measured and simulated transmitted total and reflected intensity distributions on the corresponding holographic planes at a) 5466 Hz, b) 5616 Hz and c) 5766 Hz for the stuck and separated AM3 and AM4, AM5 and AM6, AM7 and AM8.

Moreover, to discuss the influence of viscous loss on the performance of the AMs, we simulate the holographic images generated by the stuck and separated structures of AM3 and AM4 with the viscous loss of air at 5716 Hz, and both edge frequencies 5350 and 6200 Hz, (see the Supporting Information). The simulated results show that, by introducing the viscous loss, the sound instensity of holographic images decreases slightly, and the images still exist at 3 selected frequencies, indicating the robustness of the holographic images generated by the dual-layer AMs to the viscous loss. Therefore, the simulated and measured fractional bandwidths (the ratio of the bandwidth to the center frequency) for the reversal of both functions of transmitted and reflected holography generated by the 2D dual-layer aperiodic AMs can reach about 0.15 and 0.14, respectively, which is slightly lower than those type of metasurface structures with a single function of transmitted holography.[28,31] Additionally, to further demonstrate the working bandwidth of acoustic holograms, we measure the intensity distributions on both holographic planes at the edge frequencies (see the Supporting Information). We observe that the measured holographic images exist at 5280 and 6070 Hz, Therefore, the edge frequencies of the measurement are 5280 and 6070 Hz, and the measured fractional bandwidth is about 0.14, which is close to that of the simulation (about 0.15). The minor difference between both working bands may arise from the temperature of air, and the structure error of the samples in 3D printing.

In conclusion, we have theoretically proposed the GSL extension in 3D space, and experimentally designed a series of 2D dual-layer aperiodic AMs. Based on phase gradient aperiodic AMs, we realize sound abnormal refraction and reflection beyond the critical ranges for the GSL, which can be theoretically predicted by the GSL extension. Furthermore, the proposed 2D dual-layer aperiodic AMs have the ability to switch transmitted and reflected complex sound manipulations in 3D space. The measured results show that, under the excitation of a cylindrical sound source, the reversal of the sound abnormal refraction and the reflected holographic image of the curve can be realized by stucking and separating AM1 and AM2. Additionally, based on AM3-AM8, we can realize the conversion between the transmitted and reflected holograms of different letters, and the simulated and measured fractional bandwidths for both functions can reach about 0.15 and 0.14, respectively. The GSL extension in 3D space and its associated 2D aperiodic AMs provide a theoretical framework of complex wavefront manipulations in 3D space, and pave the way for designing multifunctional 3D sound devices in practice.

Experimental Section

Sample Fabrication: The samples AM1-AM8 are made of epoxy resin (Lasty-R, density 1.15 g/cm^3, Poisson's ratio 0.43, Yang's modulus 2688 MPa), and are fabricated by using 3D printing based on the technology of liquid epoxy resin photopolymerization. The models of the samples AM1-AM8 are designed by the software of COMSOL Multiphysics, and are discretized into a series of curve trajectories by a layered software. The photocurable 3D printer (UnionTech type-SLALite600, 0.1 mm in precision) controls the ultraviolet laser beam to scan along these motion trajectories on the surface of the liquid epoxy resin. The liquid epoxy resin can undergo photocurable crosslinking along these trajectories, and finally the samples AM1-AM8 are printed. The sizes of the samples are 40cm×40cm×4cm for AM1 and AM2, and 70cm×70cm×4cm for AM3-AM8. The photographs of these samples are presented in **Figure S17** (see the Supporting Information).

Experimental Set-up: The experimental set-up for measuring sound transmission and reflection are presented in **Figure S18** (see the Supporting Information). The sound-absorbing foams placed at the platform are adopted to avoid sound reflection. A loudspeaker driven by a power amplifier is used to generate incident cylindrical wave. Two microphones (Brüel&Kjær type-4954) are used to measure pressure distributions. The microphone1 can be moved flexibly with a step of 1 cm by a set of 2D motorized linear stage to measure sound signals in the scanning regions. The microphone 2 is fixed toward the loudspeaker to measure a reference signal.

Statistical Analysis: By using the software PULSE Labshop (Brüel&Kjær 3160-A-022), the transmitted pressure distributions in the scanning regions can be recorded and analyzed, and the reflected ones can be obtained by subtracting the measured pressure distributions with and without the sample. In the measurement, the detected sound signals at each position are averaged out of 30 measurements to reduce noise.

Supporting Information

Supporting Information is available from the Wiley Online Library or from the author.

Acknowledgments

This work was supported by the National Natural Science Foundation of China under Grants No. 12274183, No. 12174159, and No. 51976079, the National Key Research and Development Program of China under Grant No. 2020YFC1512403, the Research Project of State Key Laboratory of Mechanical System and Vibration under Grant No. MSV202201, the Postgraduate Research and Practice Innovation Program of Jiangsu Province under Grant No. KYCX23_3746, the Key Research and Development Program of the Ministry of Science and Technology under Grants No. 2022YFA1405200, No. 2022YFA1404704, No. 2022YFA1404902, and No. 2022YFA1404900, the National Natural Science Foundation of China under Grants No. 62175215 and No. 61975176, the Key Research and Development Program of Zhejiang Province under Grant No. 2022C01036, the Fundamental Research Funds for the Central Universities (2021FZZX001-19), the Excellent Young Scientists Fund Program (Overseas) of China, the Singapore National Research Foundation (NRF) under Grant No. NRF-CRP23-2019-0007, and the Singapore Ministry of Education (MOE) under Grant No. MOE2019-T2-2-085.

Conflict of Interest

The authors declare no conflict of interest.

Keywords

Metagratings, generalized Snell's law, phase modulation, diffraction, holography

[1] N. F. Yu, P. Genevet, M. A. Kats, F. Aieta, J. Tetienne, F. Capasso, Z. Gaburro, *Science* **2011**, 334, 333.

[2] X. J. Ni, N. K. Emani, A. V. Kildishev, A. Boltasseva, V. M. Shalaev, *Science* **2012**, 335, 427.

[3] X. B. Yin, Z. L. Ye, J. Rho, Y. Wang, X. Zhang, *Science* **2013**, 339, 1405.

[4] T. J. Cui, M. Q. Qi, X. Wan, J. Zhao, Q. Cheng, *Light: Sci. Appl.* **2014**, 3, e218.

[5] D. M. Lin, P. Fan, E. Hasman, M. L. Brongersma, *Science* **2014**, 345, 298.

[6] N. F. Yu, F. Capasso, *Nat. Mater.* **2014**, 13, 139.

[7] Y. D. Xu, Y. Y. Fu, H. Y. Chen, *Nat. Rev. Mater.* **2016**, 1, 16067.

[8] K. W. Allen, D. J. P. Dykes, D. R. Reid, R. T. Lee, *Prog. Electromagn. Res.* **2020**, 167, 19.

[9] Y.-S. Choi, S. Lee, J.-Y. Jung, K.-Y. Jeong, H.-G. Park, M.-K. Seo, *Adv. Optical Mater.* **2020**, 8, 1901970.

[10] Y. Q. Liu, Z. X. Liang, F. Liu, O. Diba, A. Lamb, J. Li, *Phys. Rev. Lett.* **2017**, 119, 034301.

[11] M. S. Kim,W. R. Lee, Y. Y. Kim, J. H. Oh, *Appl. Phys. Lett.* **2018**, 112, 241905.

[12] L. Y. Cao, Z. C. Yang, Y. L. Xu, S.-W. Fan, Y. F. Zhu, Z. L. Chen, B. Vincent, B. Assouar, *Phys. Rev. Appl.* **2020**, 13, 014054.

[13] M. Y. Zheng, C. I. Park, X. N. Liu, R. Zhu, G. K. Hu, Y. Y. Kim, *Appl. Phys. Lett.* **2020**, 116, 171903.

[14] J. J. Rong, W. J. Ye, S. Y. Zhang, Y. J. Liu, *Adv. Funct. Mater.* **2020**, 30, 2005285.

[15] T. Yang, Z. B. Lin, X. F. Zhu, T. Z. Yang, *Phys. Rev. Appl.* **2022**, 18, 064065

[16] H.-W. Dong, S.-D. Zhao, M. Oudich, C. Shen, C. Z. Zhang, L. Cheng, Y.-S. Wang, D. Fang, *Phys. Rev. Appl.* **2022**, 17, 044013.

[17] K. Stojanoska, C. Shen, *Appl. Phys. Lett.* **2022**, 120, 241701.

[18] B. Assouar, B. Liang, Y. Wu, Y. Li, J. C. Cheng, Y. Jing, *Nat. Rev. Mater.* **2018**, 3, 460.

[19] Y. Li, B. Liang, Z. M. Gu, X. Y. Zou, J. C. Cheng, *Sci. Rep.* **2013**, 3, 2546.

[20] Y. B. Xie, A. Konneker, B.-I. Popa, S. A. Cummer, *Appl. Phys. Lett.* **2013**, 103, 201906.

[21] K. Tang, C. Y. Qiu, M. Z. Ke, J. Y. Lu, Y. T. Ye, Z. Y. Liu, *Sci. Rep.* **2014**, 4, 6517.

[22] J. Mei, Y. Wu, *New J. Phys.* **2014**, 16, 123007.

[23] X. Jiang, Y. Li, B. Liang, J. C. Cheng, L. K. Zhang, *Phys. Rev. Lett.* **2016**, 117, 034301.

[24] B. Y. Xie, K. Tang, H. Cheng, Z. Y. Liu, S. Q. Chen, J. G. Tian, *Adv. Mater.* **2017**, 29, 1603507.

[25] Z. H. Tian, C. Shen, J. F. Li, E. Reit, Y. Y. Gu, H. Fu, S. A. Cummer, T. J. Huang, *Adv. Funct. Mater.* **2019**, 29, 1808489.

[26] L. Quan, A. Alù, *Phys. Rev. Lett.* **2019**, 123, 244303.

[27] K. Melde, A. G. Mark, T. Qiu, P. Fischer, *Nature* **2016**, 537, 518.

[28] Y. B. Xie, C. Shen, W. Q. Wang, J. F. Li, D. J. Suo, B.-I. Popa,Y. Jing, S. A. Cummer, *Sci. Rep.* **2016**, 6, 35437.

[29] Y. F. Zhu, J. Hu, X. D. Fan, J. Yang, B. Liang, X. F. Zhu, J. C. Cheng, *Nat. Commun.* **2018**, 9, 1632.

[30] Y. Y. Gu, C. Y. Chen, J. Rufo, C. Shen, Z. Y. Wang, P.-H. Huang, H. Fu, P. Zhang, S. A Cummer, Z. H. Tian, T. J. Huang, *ACS Nano* **2020**, 14, 14635.

[31] M. X. Xu, W. S. Harley, Z. C. Ma, P. V. S. Lee, D. J. Collins, *Adv. Mater.* **2023**, 35, 2208002.

[32] Y. B. Xie, W. Q. Wang, H. Y. Chen, A. Konneker, B. I. Popa, S. A. Cummer, *Nat. Commun.* **2014**, 5, 5553.

[33] Y. Ra'di, D. L. Sounas, A. Alù, *Phys. Rev. Lett.* **2017**, 119, 067404.

[34] Y. Ra'di, A. Alù, *ACS Photonics* **2018**, 5, 1779.

[35] V. Popov, F. Boust, S. N. Burokur, *Phys. Rev. Appl.* **2018**, 10, 011002.

[36] V. Neder, Y. Ra'di, A. Alù, A. Polman, *ACS Photonics* **2019**, 6, 1010.

[37] Y. H. Wang, Y. Cheng, X. J. Liu, *Sci. Rep.* **2019**, 9, 7271.

[38] S. L. Sun, K. Y. Yang, C. M. Wang, T. Juan, W. T. Chen, C. Y. Liao, Q. He, S. Y. Xiao, W. T. Kung, G. Y. Guo, L. Zhou, D. P. Tsai, *Nano Lett.* **2012**, 12, 6223.

[39] A. Pors, M. G. Nielsen, S. I. Bozhevolnyi, *Optica* **2015**, 2, 716.

[40] F. Ding, Z. Wang, S. He, V. M. Shalaev, A. V. Kildishev, *ACS Nano* **2015**, 9, 4111.

[41] N. M. Estakhri, A. Alù, *Phys. Rev. X* **2016**, 6, 041008.

[42] M. Li, L. Q. Jing, X. Lin, S. Xu, L. Shen, B. Zheng, Z. J. Wang, H. S. Chen, *Adv. Optical Mater.* **2019**, 7, 13.

[43] B. Y. Liu, B. Ren, J. J. Zhao, X. D. Xu, Y. X. Feng, W. Y. Zhao, Y. Y. Jiang, *Appl. Phys. Lett.* **2017**, 111, 221602.

[44] Y. Y. Fu, C. Shen, Y. Y. Cao, L. Gao, H. Y. Chen, C. T. Chan, S. A. Cummer, Y. D. Xu, *Nat. Commun.* **2019**, 10, 2326.

[45] Y. Y. Fu, C. Shen, X. H. Zhu, J. F. Li, Y. W. Liu, S. A. Cummer, Y. D. Xu, *Sci. Adv.* **2020**, 6, eaba9876.

[46] Y. Y. Fu, Y. Tian, X. Li, S. l. Yang, Y. W. Liu, Y. D. Xu, M. H. Lu, *Phys. Rev. Lett.* **2022**, 128, 104501.

[47] J. Qian, J. P. Xia, H. X. Sun, Y. Wang, Y. Ge, S. Q. Yuan, Y. H. Yang, X. J. Liu, B. L. Zhang, *Adv. Mater. Technol.* **2020**, 5, 2000542.

[48] Y. J. Lu, H. Y. Zou, J. Qian, Y. Wang, Y. Ge, S. Q. Yuan, H. X. Sun, X. J. Liu, *Appl. Phys. Lett.* **2021**, 119, 173501.

[49] J. Qian, Y. Wang, S. Q. Yuan, H. X. Sun, X. J. Liu, *Appl. Phys. Express* **2019**, 12, 094001.